

Electronic Properties of MoS₂–WS₂ Heterostructures Synthesized with Two-Step Lateral Epitaxial Strategy

Kun Chen,^{†,‡} Xi Wan,^{†,‡} Jinxiu Wen,[‡] Weiguang Xie,[§] Zhiwen Kang,[†] Xiaoliang Zeng,^{||}
Huanjun Chen,[‡] and Jian-Bin Xu^{*,†}

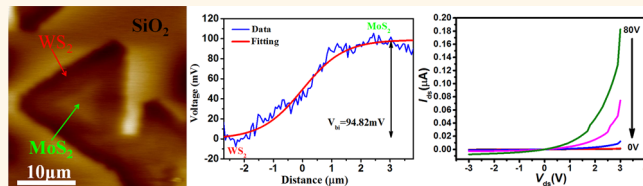
[†]Department of Electronic Engineering and Materials Science and Technology Research Center, The Chinese University of Hong Kong, Hong Kong, SAR P. R.

China, [‡]State Key Laboratory of Optoelectronic Materials and Technologies and Guangdong Province Key Laboratory of Display Material and Technology,

School of Physics and Engineering, Sun Yat-sen University, Guangzhou 510275, China, [§]Siyuan Laboratory, Department of Physics, Jinan University,

Guangzhou 510632, China, and ^{||}Shenzhen Institutes of Advanced Technology, Chinese Academy of Sciences, Shenzhen 518055, China. [†]These authors contributed equally to this work.

ABSTRACT Formation of heterojunctions of transition metal dichalcogenides (TMDs) stimulates wide interest in new device physics and technology by tuning optical and electronic properties of TMDs. TMDs heterojunctions are of scientific and technological interest for exploration of next generation flexible electronics. Herein, we report on a two-step epitaxial ambient-pressure CVD



technique to construct in-plane MoS₂–WS₂ heterostructures. The technique has the potential to artificially control the shape and structure of heterostructures or even to be more potentially extendable to growth of TMD superlattice than that of one-step CVD technique. Moreover, the unique MX₂ heterostructure with monolayer MoS₂ core wrapped by multilayer WS₂ is obtained by the technique, which is entirely different from MX₂ heterostructures synthesized by existing one-step CVD technique. Transmission electron microscopy, Raman and photoluminescence mapping studies reveal that the obtained heterostructure nanosheets clearly exhibit the modulated structural and optical properties. Electrical transport studies demonstrate that the special MoS₂ (monolayer)/WS₂ (multilayer) heterojunctions serve as intrinsic lateral p–n diodes and unambiguously show the photovoltaic effect. On the basis of this special heterostructure, depletion-layer width and built-in potential, as well as the built-in electric field distribution, are obtained by KPFM measurement, which are the essential parameters for TMD optoelectronic devices. With further development in future studies, this growth approach is envisaged to bring about a new growth platform for two-dimensional atomic crystals and to create unprecedented architectures therefor.

KEYWORDS: two-step epitaxial CVD method · MoS₂–WS₂ heterostructure · KPFM · depletion-layer width · built-in potential · built-in electric field

Heterostructures formed by interfacing two different materials with various geometrical and electronically energetic alignments yield tremendous significance for fundamental and applied interests.^{1–3} It is a cornerstone for developing high-speed electronics and optoelectronic devices with emergent properties.^{4,5} Traditionally, the properties of conventional semiconductor heterostructures fabricated by epitaxial growth techniques are often limited by the difficulty in realizing high-quality interfaces where, oftentimes, a slight lattice mismatch results in the poor interface qualities. Two-dimensional (2-D) semiconductors, such as transition metal dichalcogenides (TMDs),⁶ have attracted broad attention in recent years because of their

unique structures, versatile electronic and optical properties, and potential applications.^{6–9} Although these TMDs share the same crystalline structure, their physical properties, e.g., bandgap, light–matter interaction, and spin–orbit coupling strength, vary significantly. An intriguing possibility of epitaxial growth in 2-D layered semiconductors, due to apt lattice match of TMDs with different bandgaps and workfunctions, opens up a new avenue for unprecedented lateral heterostructures.^{10–15} The interface can be atomically sharp and the junction region can be as thin as one atomic layer. These systems are fundamentally different and more flexible than traditional heterostructures composed of conventional semiconductors. 2-D lateral heterostructures have

* Address correspondence to jbxu@ee.cuhk.edu.hk.

Received for review May 26, 2015
and accepted September 16, 2015.

Published online September 16, 2015
10.1021/acsnano.5b03188

© 2015 American Chemical Society

revealed some novel properties and phenomena that could create a new paradigm in architecture design of heterostructures for future nanoelectronic devices with large-scale integration.^{11–14,16} Up until now, chemical vapor deposition (CVD) has proven to be the most promising technique for synthesis of 2-D lateral heterostructures with high quality. Very recently, in-plane heterostructure TMDs, namely MoS₂–WS₂,^{11,12} WS₂–WSe₂,¹⁴ and MoSe₂–WSe₂,^{11,13} have been synthesized by one-step CVD growth technique. However, the reliable growth of TMD lateral heterostructures is still a considerable challenge and the existing growth process and experimental setups are not easily accessible; in addition, some special precursors are needed, which may not be commonly accessible for research and development of 2-D heterostructures. Moreover, the in-plane TMDs heterostructures synthesized by the existing single-step growth technique are significantly self-assembled. Therefore, it is rather difficult to intentionally control the shapes and structures of the resulting heterostructures, which greatly impedes the facile device fabrication and integration. Here, we demonstrate two-step lateral epitaxial strategy to achieve lateral heteroepitaxy of WS₂ to MoS₂ synthesized beforehand with a good repeatability. With this technique, the growth process and experimental setup can be remarkably simplified. In addition, with further development in future, MoS₂ can be patterned in different shapes as intended before heteroepitaxy. Subsequently, the lateral epitaxial approach may be extended to the growth of various shapes of lateral TMDC heterojunctions,¹⁷ even superlattice structures consisting of two or more two-dimensional layered materials with greater complexity and more functionalities, which could unravel a new door to exotic physics and/or totally new device concepts. The lateral WS₂–MoS₂ heterostructures obtained by this two-step lateral epitaxial strategy are verified by Raman spectroscopy, photoluminescence (PL) spectroscopy, and transmission electron microscopy (TEM). Electronic transport studies demonstrate that the special MoS₂ (monolayer)/WS₂ (multilayer) heterojunctions serve as intrinsic lateral p–n diodes and photodiodes. In addition, the electrical potential distribution of lateral WS₂–MoS₂ heterostructure is characterized by Kelvin probe force microscopy (KPFM). On the basis of KPFM measurement, depletion-layer width and built-in potential, as well as the built-in electric field distribution of the lateral heterostructure, are estimated, which are the important parameters for the lateral heterostructure devices.

RESULTS AND DISCUSSION

Figure 1a schematically illustrates the experimental setup for growth of WS₂/MoS₂ lateral heterostructures with two-step lateral epitaxial growth strategy. The MoS₂ nanosheets were first synthesized on a clean SiO₂/Si substrate using traditional ambient-pressure

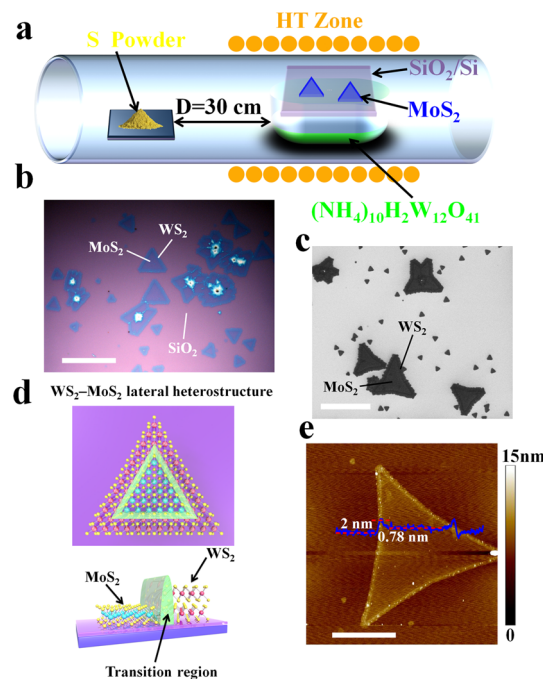
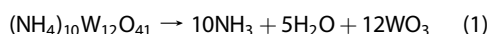


Figure 1. Schematic of experimental setup and overall morphologies of the lateral WS₂/MoS₂ heterostructures synthesized with two-step lateral epitaxial growth (two-step WS₂/MoS₂ heterostructures). (a and d) Schematic illustrations of (a) home-built two-step APCVD setup and (d) WS₂/MoS₂ in-plane heterojunctions. (b) Optical image of triangular or star crystals wrapped by the relatively bright edges showing the lateral heterostructures. Scale bar: 30 μm . (c) SEM image of heterostructure crystals. Scale bar: 30 μm . (e) AFM image of a triangular domain showing a core region with the thickness of 0.78 nm and a shell region with the thickness of 2 nm. Scale bar: 10 μm .

chemical vapor deposition (APCVD) with molybdenum trioxide (MoO₃) powder as the precursors (Supporting Information S1). Then, in the lateral heteroepitaxy of WS₂, ammonium tungstate hydrate $(\text{NH}_4)_{10}\text{W}_{12}\text{O}_{41} \cdot x\text{H}_2\text{O}$ was used as starting reactant. First, $(\text{NH}_4)_{10}\text{W}_{12}\text{O}_{41} \cdot x\text{H}_2\text{O}$ powders were dissolved in deionized (DI) water to form 10 mg/mL solution. Then, 10 mL of ammonium tungstate solution was dipped into a quartz boat, followed by a heating process at 250 °C for 1 h to remove the solvent. The reason for this step is to form a homogeneous thin layer of ammonium tungstate in the quartz boat. The SiO₂/Si substrate with MoS₂ nanosheets was mounted on the top of the quartz boat placed in the middle of a 1-in. quartz tube reaction chamber, with MoS₂ facing down to the ammonium tungstate. During this process, to avoid the potential contaminations from the external environment as much as possible, the sample was quickly put into another furnace for the second step WS₂ growth, with sulfur powder (0.8 g) placed upstream 30 cm away from the center of a the quartz tube. Before heating, the furnace was pre-evacuated down to 50 mTorr and backfilled with Ar (99.999% purity) to ambient pressure. This clean cycle was repeated 3–5 times to remove the absorbed water molecules. Then, the whole CVD system was

purged with 500 sccm Ar for 20 min. After that, the system was ramped to 850 °C at a rate of 30 °C/min, and remained at 850 °C for the lateral epitaxial growth of WS₂ for about 20 min under the atmospheric pressure with a mixture of argon and hydrogen (10% hydrogen), at a flow rate of 100 sccm. When the growth was terminated, 500 sccm Ar flow was introduced into the furnace to remove the residual reactants and the sample was rapidly cooled to room temperature by pushing out of the hot zone of the furnace. The thermolysis of ammonium tungstate (NH₄)₁₀W₁₂O₄₁ in an inert gas environment resulted in the conversion of (NH₄)₁₀W₁₂O₄₁ to WO₃ at above 600 °C,¹⁸ as described by eq 1.



The as grown WS₂–MoS₂ in-plane heterostructures were characterized by optical microscopy, scanning electron microscopy (SEM), and atomic force microscopy (AFM). The schematics and typical configuration of two-step lateral epitaxial WS₂–MoS₂ heterostructures are shown in Figure 1b–e, where the lateral interfaces between WS₂ and MoS₂ were easily distinguished by the contrast difference in optical image (Figure 1b). Single-layer MoS₂ nanosheets (identified by Raman and PL in the following section) (triangular or star-like crystals) were wrapped by the relatively bright multilayer WS₂ peripheral edges with sharp 1D heterointerfaces. The particular morphology of the heterostructures was further verified by AFM images. Figure 1e shows typical AFM image of an as-grown heterostructure, indicating a flat surface over the entire triangle core region with a thickness of 0.78 nm¹² and a thicker shell region with a thickness of 2 nm. This is a further evidence that the multilayer WS₂ (shell) was laterally epitaxially welded on the monolayer MoS₂ nanosheets (core). The morphology and structure of WS₂–MoS₂ heterostructure obtained by two-step lateral epitaxial growth strategy are completely different from those synthesized by one-step CVD method,^{12–14} which show the monolayer nature of the heterostructures. We assume that this significant distinction is due to the different underlying growth mechanism. For one-step growth strategy, there is no break between the growth of the core and shell region and the whole process maintains at a higher temperature. Therefore, the growth fronts could keep active during the whole growth process and steadily move forward, which would result in a flat and smooth monolayer of heterostructure. However, in two-step growth strategy, the core region is synthesized first; hence, the edges of the core layer will be cooled to a lower energetically stable state. Subsequently, during the second heteroepitaxy process at high temperature, the state of the core layer's edges will be reactivated to become growth fronts, which will cause some defects during this process. These defects with higher energies will serve as the nucleation centers in the heteroepitaxial process, which will capture abundant adatoms and then

lead to the lateral epitaxy of the multilayer shell material surrounding on the core material edges. Eventually, the special heterostructures with particular morphology and structure were generated. It could be found that, in some cases, as the WS₂ shell regions further extended, the growth fronts would gradually move away from the nucleation centers and the thickness of WS₂ would become monolayer. Finally, a ring of protuberant interface between MoS₂ and WS₂ could be clearly observed (Supporting Information S2). At this stage, the precise growth process and underlying mechanism are still unclear, which requires careful investigation in future work.

The structural and optical properties in the as-grown lateral heterostructures were spatially investigated by Raman spectroscopy and photoluminescence (PL) spectroscopy. Figures 2a and 2b show the optical image and SEM micrograph of the WS₂–MoS₂ lateral heterojunction used for Raman and PL characterization. Distinct features of Raman spectra taken from the central and surrounding regions of a triangular domain (in Figure 2a) are clearly shown in Figure 2c. The Raman spectrum from the core region (green dot) shows characteristic resonance peaks of monolayer MoS₂, with the out-of-plane A_{1g} mode at 401.2 cm⁻¹ and the in-plane E_{2g} mode at 381.4 cm⁻¹ (green line in Figure 2c),^{19,20} while the Raman spectrum taken in the peripheral layer (red dot) shows clear peaks at 350.7 and 418.4 cm⁻¹ (red line in Figure 2c), consistent with the 2 LA(M) and A_{1g} resonance modes of bilayer WS₂.^{21–24} These micro-Raman studies demonstrate that the two distinct materials coexist within the same triangular domain. The Raman mapping analysis can further reveal the spatial distributions within the triangular domain, with a triangular monolayer MoS₂ domain existing in the core region (Figure 2f), while WS₂ is in the shell layer (Figure 2g). A combined Raman mapping image shows the seamless lateral integration of MoS₂ and WS₂ in the heterostructure domain (Figure 2e) with seemingly clear interface within the mapping resolution. Similarly, micro-PL studies also show characteristic photoluminescence peaks at ~677 nm for the inner layer and ~638 nm for the outer layer (Figure 2d), in agreement of the near- band-edge (NBE) emission from MoS₂ and WS₂, respectively.^{25,26} The peak intensity of 638 nm is much suppressed for the bilayered WS₂.^{23,27,28} The PL mapping studies (Figures 2h–2j) have features similar to those of Raman mapping images, further confirming this unique core–shell structure. Due to the large laser spot size (~1 μm) and the mapping step size of 200 nm, the in-plane interface of the heterostructure in the Raman and PL mappings appears to be slightly diffused, which results in the atomically abrupt heterojunction cannot be determined accurately. Within the limit of optical resolution, these Raman and PL mapping studies indicate that the MoS₂ inner triangle and WS₂ peripheral areas are well laterally coherent.

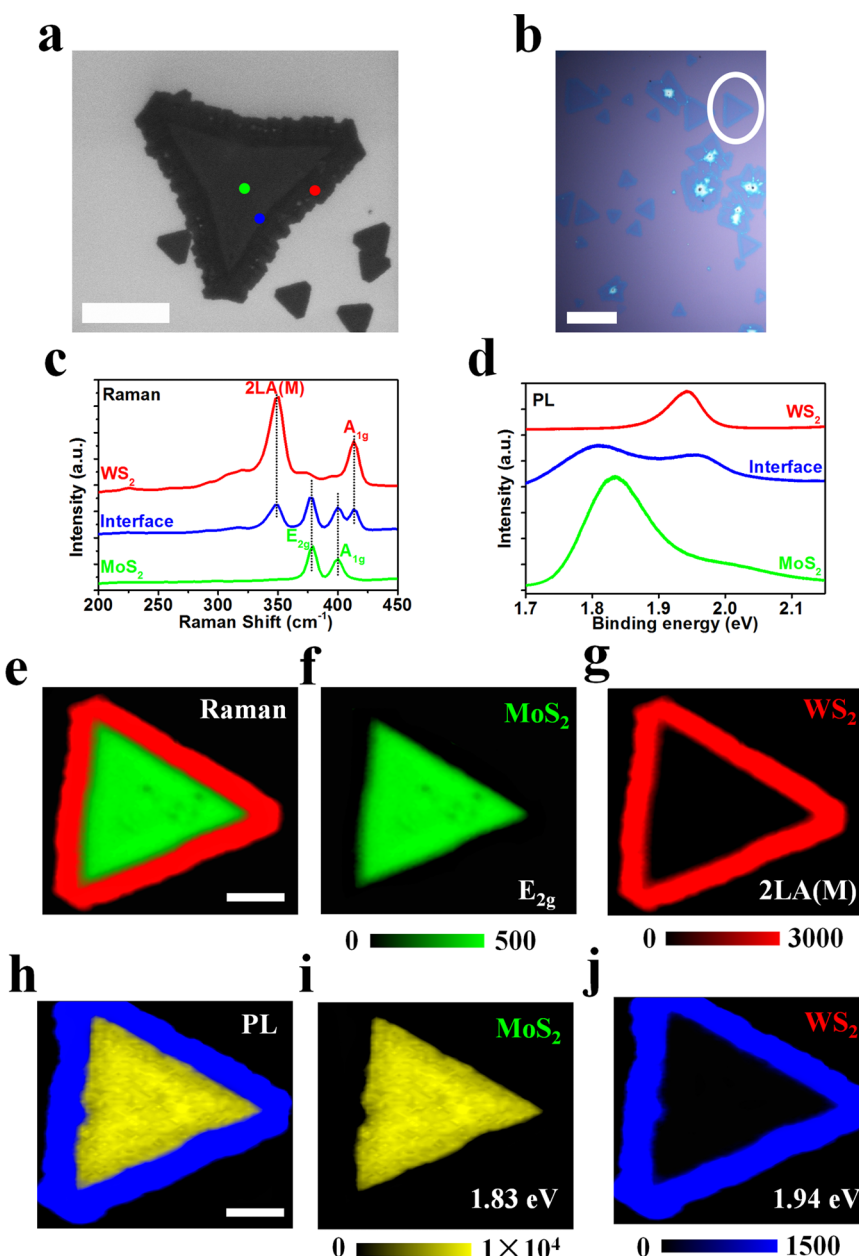


Figure 2. Raman and photoluminescence (PL) characterization of two-step WS_2/MoS_2 lateral heterostructures. (a and b) SEM micrograph and optical image of the WS_2-MoS_2 lateral heterojunction used for Raman and PL characterization (scale bars in (a), 10 μm ; scale bars in (b), 40 μm). (c) Raman spectra and (d) PL spectra of WS_2 , MoS_2 and interfacial areas in the heterostructure domain as marked in panel a. The green curves show the characteristic Raman and PL peaks of MoS_2 obtained from the inner triangle. The red curves show the characteristic WS_2 Raman and PL peaks obtained from the outer triangle. And the blue curves obtained at the interface area show the superposition of MoS_2 and WS_2 signals. (f) Raman mapping at 381 cm^{-1} (MoS_2 E_{2g} mode) and (g) Raman mapping at 418.3 cm^{-1} (WS_2 A_{1g} mode), demonstrating that MoS_2 is presented in the center triangle and WS_2 is located in the surrounding areas of the triangular domain. (e) Combined Raman intensity mapping at 418.3 cm^{-1} (red) and 381 cm^{-1} (green), indicating the good lateral interconnection of the MoS_2 center triangle and the WS_2 outer shell. (i and j) PL intensity mapping images at 677 and 638 nm corresponding to the characteristic PL peaks of MoS_2 and WS_2 , respectively. Consistent with the Raman mapping, MoS_2 is in the core region and WS_2 is in shell area of the triangular heterostructure. (h) Combined PL intensity mapping at 677 nm (yellow) and 638 nm (blue), demonstrating the formation of WS_2/MoS_2 lateral heterostructures, consistent with Raman mapping studies (scale bars in (e) and (h), 10 μm ; scale bars in (e) and (h) apply to (f), (g), (i), (j)).

Transmission electron microscopy (TEM), combined with selected area electron diffraction (SAED), was used to investigate the crystallinity of the synthesized WS_2-MoS_2 in-plane heterostructure at atomic scale. Figure 3a shows an optical micrograph of a WS_2-MoS_2

heterostructure transferred onto a holey SiN TEM grid. Figure 3b–d show the high-resolution (HR) TEM images and the selected SAED patterns corresponding to the numbered color holes in Figure 3a. The typical 6-fold spot diffraction pattern and high quality lattice

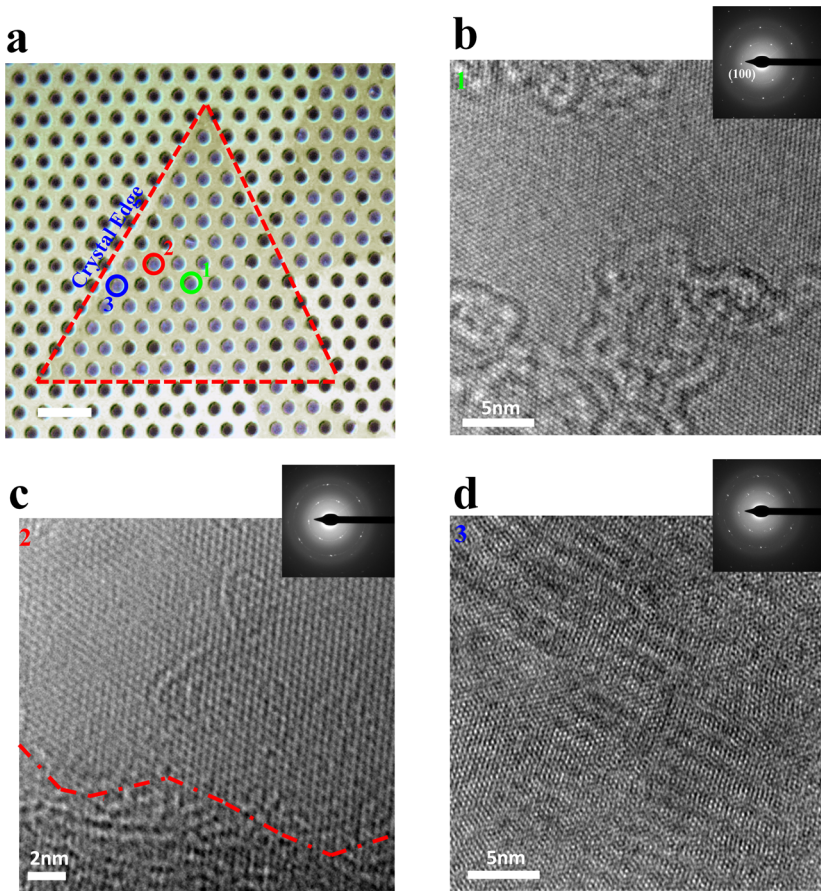


Figure 3. Structure of WS_2/MoS_2 lateral heterostructures. (a) Optical microscopy image of a region of the WS_2/MoS_2 heterojunction domain transferred onto a holey SiN TEM grid. Scale bar: $4\ \mu\text{m}$. The high-resolution (HR) TEM images and the selected SAED diffraction patterns taken from region 1, the MoS_2 monolayer core region (b); region 2, the interface (c); and region 3, the multilayer WS_2 peripheral region (d) marked in (a).

structure shown in Figure 3b implies a single MoS_2 monolayer crystal lattice (D_{3h} point group symmetry) of the core region. The interface between monolayer MoS_2 core region and multilayer WS_2 peripheral layer (red dash line in Figure 3c) and some defects/distortion around the interface can be observed from Figure 3c and the diffraction pattern reveals the superposition of MoS_2 and WS_2 lattice. The defects/distortion might be formed by the reactivating process of the core layer's edges to become growth fronts during the second heteroepitaxy (as we assumed above) or due to the lateral lattice mismatch¹⁷ between monolayer MoS_2 and multilayer WS_2 . The HR-TEM micrograph taken from WS_2 peripheral region (Figure 3d) shows the typical atomic-scale Moiré patterns of multilayer structures.²⁹ In addition, the diffused diffraction pattern could be due to the crystallographic misorientations of multilayer WS_2 as well as its tiny disordered structure.

The electronic properties of the lateral heterostructures under thermal equilibrium, such as depletion-layer width and built-in potential, as well as the built-in electric field distribution, which are key parameters for future optoelectronic applications, have been estimated by Kelvin probe force microscope (KPFM) study.

The mapping of the work function by KPFM provides the information about the composition and electronic states of the local structures of the WS_2-MoS_2 in-plane heterostructure. Importantly, the Fermi levels of WS_2 or MoS_2 in the heterostructure can be estimated from the surface potential map, so as to obtain the scale of the space charge region, the value of built-in potential and so on. The contact potential difference (CPD) between the AFM tip and the local area of WS_2 or MoS_2 can be written as

$$\text{CPD}_{\text{WS}_2} = \phi_{\text{tip}} - \phi_{\text{WS}_2} \quad (2)$$

$$\text{CPD}_{\text{MoS}_2} = \phi_{\text{tip}} - \phi_{\text{MoS}_2} \quad (3)$$

where ϕ_{tip} , ϕ_{WS_2} , and ϕ_{MoS_2} are the work functions of the tip, WS_2 , and MoS_2 , respectively. The topographic image and its compounding surface potential distribution of a WS_2-MoS_2 in-plane heterostructure are shown in Figure 4, panels a and b, respectively. From Figure 4a, it can be found that bilayer MoS_2 (with the thickness of 1.7 nm) were merged on the core edges of monolayer MoS_2 nanosheets (with the thickness of 0.8 nm) by epitaxially lateral growth. Owing to the work function difference between bilayer WS_2 and

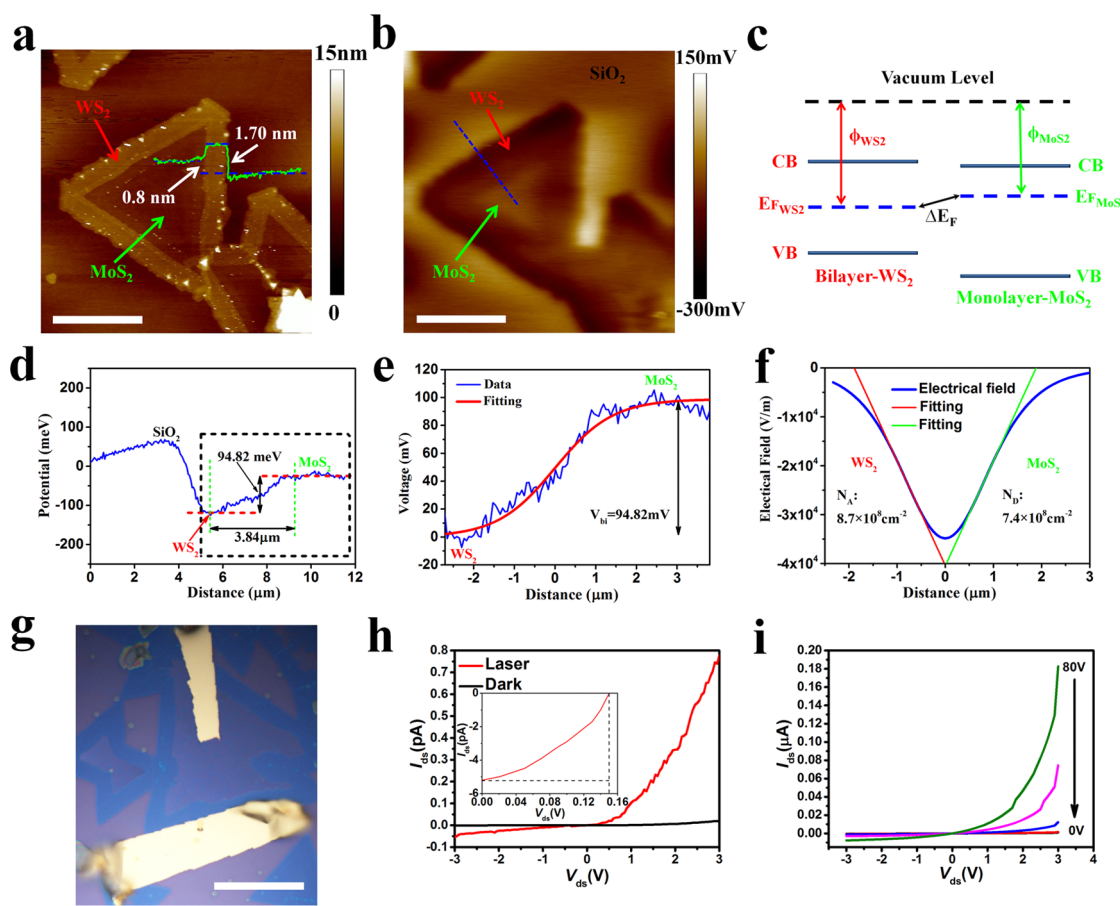


Figure 4. (a) AFM image and (b) KPFM surface potential map of a triangular heterostructure domain. Scale bar: 10 μm . The AFM image indicates that a monolayer MoS₂ (0.8 nm) is embroidered by bilayer WS₂. The surface potential interface of the lateral heterostructure is observed in KPFM image due to the work function difference of monolayer MoS₂ and bilayer WS₂. (c) Schematic of Band profiles of monolayer MoS₂ and bilayer WS₂, which forms a type II heterojunction. (d) Plot of the surface potential measured along the blue dash line depicted in panel b and the region of WS₂/MoS₂ lateral heterostructure is in the dotted box. (e) The built-in potential distribution across the heterostructure corresponding to the region in the dotted box of panel d. (f) The built-in electric field distribution of WS₂/MoS₂ lateral heterostructure. (g) Optical image for the WS₂/MoS₂ heterostructure device; scale bar: 15 μm . (h) Experimental I–V curve of the lateral WS₂/MoS₂ heterojunction diode in the dark (black line) and under illumination (red line; wavelength, 514 nm; power, 1 mW). Inset is photovoltaic effect. (i) Gate-tunable output characteristics of a WS₂/MoS₂ heterojunction diode. The gate voltage varies from 80 to 0 V in steps of 20 V.

monolayer MoS₂, the surface potential interface and depletion region of the lateral heterostructure can be observed from KPFM image. Due to the long depletion region, the contrast feature of KPFM image is slightly different from the topographic image (Figure 4a). The difference between the Fermi levels of WS₂ and MoS₂ is obtained by measuring the $\Delta\text{CPD}_{\text{WS}_2-\text{MoS}_2}$ on average (Figures 4c and 4d), which here is defined as

$$\begin{aligned} \Delta E_F &= E_{F_{\text{WS}_2}} - E_{F_{\text{MoS}_2}} = \Delta \text{CPD}_{\text{WS}_2 - \text{MoS}_2} \\ &= \text{CPD}_{\text{WS}_2} - \text{CPD}_{\text{MoS}_2} = \phi_{\text{MoS}_2} - \phi_{\text{WS}_2} \end{aligned} \quad (4)$$

The value $\Delta E_F \sim 95$ meV and the depletion-layer width $W \sim 3.84 \mu\text{m}$ can be observed from a typical line profile of the surface potential (Figure 4d) (the blue dash line in Figure 4b). From Figures 4c and 4d, we found that the Fermi levels of the core monolayer MoS₂ are higher than those of the shell bilayer WS₂ about 95 meV. Therefore, when WS₂ and MoS₂ form a lateral

heterostructure, electrons will diffuse from MoS₂ to WS₂. The MoS₂–WS₂ heterostructure forms a type II heterojunction^{30,31} (if we neglect the hybridization of electronic states in the MoS₂ and WS₂ layers), with the conduction band minimum residing in MoS₂ and the valence band maximum in WS₂, respectively (Figure 4c). The lateral WS₂–MoS₂ heterostructures can serve as intrinsic monolayer p–n junctions, where WS₂ serves as p-side and MoS₂ serves as n-side. The built-in potential or the built-in electric field of the heterojunction will lead to efficient charge transfer, with the separated electrons and holes residing in two regions that can have a dominating effect on both photovoltaic responses and light emission in MoS₂–WS₂ heterostructures. Figure 4e shows the built-in potential distribution across the heterostructure, which can be easily obtained through surface potential profile. Here, only the region of WS₂–MoS₂ lateral heterostructure in the dotted box of Figure 4d is considered, where the

potential of bilayer WS₂ and the midpoint of depletion region are set to zero. The built-in potential is found to be ~95 mV, which is underestimated¹⁷ compared to the open-circuit voltage V_{OC} of ~0.15 V obtained by photovoltaic measurement (Figure 4h) due to the effect of the surface adsorbates,³² but the value is still reasonable. The distribution of built-in potential is well fitted by a sigmoid function (in Figure 4e):^{33,34}

$$y = \frac{a}{1 + e^{-x/b}} \quad (5)$$

where $a = 97.2$ mV, which is very close to the measured value (95 mV) of the built-in potential, and $b = 0.71$. Then, the built-in electric field distribution can be obtained by differentiating the fitting profile of the built-in potential shown in Figure 4f. The direction of built-in electric field is from WS₂ to MoS₂ regions and the maximum field $\xi_m(x)$ that exists at the midpoint of depletion region is 34.9 mV/μm. From the shape of electric field distribution, it can be estimated that the lateral WS₂–MoS₂ heterostructure p–n junction is close to the abrupt junction.³⁰ The electric field $\xi(x)$ of classic 2D abrupt junction can be defined as^{30,35,36}

$$\xi_{WS_2}(x) \sim -\frac{qN_A(x + W_p)}{\varepsilon_{WS_2}\varepsilon_0\rho_{WS_2}}, \quad (-W_p < x < 0) \quad (6)$$

$$\xi_{MoS_2}(x) \sim \frac{qN_D(x - W_n)}{\varepsilon_{MoS_2}\varepsilon_0\rho_{MoS_2}}, \quad (0 < x < W_n) \quad (7)$$

where $\varepsilon_{WS_2} = 6.1$ and $\varepsilon_{MoS_2} = 4.8$ are, respectively, the relative dielectric constant of bilayer WS₂ and monolayer MoS₂.³⁷ ε_0 is the vacuum permittivity, q is the elementary charge. N_D is n-type intrinsic doping concentration in WS₂ and N_A is p-type intrinsic doping concentration in MoS₂, respectively. ρ_{WS_2} and ρ_{MoS_2} are the screening lengths, which are given by $\rho_{WS_2} = 2\pi\chi_{WS_2}$ and $\rho_{MoS_2} = 2\pi\chi_{MoS_2}$, where $\chi_{WS_2} = 0.603$ nm and $\chi_{MoS_2} = 0.66$ nm are the polarizability values of monolayer WS₂ and MoS₂, respectively.³⁸ W_n is n-type depletion width, while W_p is p-type depletion width. By using eqs 6 and 7 to fit the left part and right part of electric field distribution curve, respectively, we obtain that the intrinsic n-type doping concentration N_A in WS₂ is about 8.7×10^8 cm⁻², while the intrinsic p-type doping concentration N_D in MoS₂ is about 7.4×10^8 cm⁻². Actually, both MoS₂ and WS₂ are n-type semiconductors with a tiny difference in their intrinsic doping levels. When a lateral heterostructure formed, only a few net electrons diffuse from MoS₂ (serving as n-side) to WS₂

(serving as p-side) due to the slight difference of the Fermi levels (measured by KPFM) between them. The amount of net electrons ($N_D \sim 10^9$ cm⁻²) is only a small part of the intrinsic carriers of MoS₂. This result is quite reasonable compared to the intrinsic carrier concentrations ($\sim 10^{10}$ cm⁻²) reported in the previous literature.³⁹ In addition, the total depletion width is $W = W_n + W_p = 1.9 + 1.88 = 3.78$ μm, which is self-consistent with the value ($W \sim 3.84$ μm) measured from the surface potential profile (Figure 4d). Finally, the intrinsic p–n junction nature of the lateral MoS₂/WS₂ heterostructure is further verified by electrical transport studies across a heterojunction device. The I_{ds} – V_{ds} curves of the lateral WS₂/MoS₂ heterojunction p–n diode were depicted in Figure 4h, with and without laser illumination (514 nm, 1 mW), from which the photovoltaic effect with an open-circuit voltage $V_{OC} \sim 0.15$ V and short-circuit current $I_{SC} \sim 5.2$ pA under light illumination can be observed as shown in the inset of Figure 4h. Typical current rectification behavior as in the I_{ds} – V_{ds} curves (Figure 4i) can be clearly observed, with the current only able to pass through the device when the p-type WS₂ is positively biased. The observation of current rectification clearly demonstrates a p–n diode is formed within the WS₂/MoS₂ lateral heterostructure. Under different backgate voltage ($V_g = 0$ –80 V), the output curves of the diode (I_{ds} – V_{ds}) show that the output current increases with increasing positive gate voltage, indicating that the charge transport is partly limited by the n-type the monolayer MoS₂,¹⁴ which might be duo to its relatively high Fermi level as compared to WS₂ as well as its large scale size in our devise (Figure 4g).

CONCLUSIONS

In summary, we have demonstrated a two-step lateral epitaxial CVD technique to synthesize MoS₂/WS₂ heterostructures through a facile growth process and experimental setup. It has more potential to artificially control the shape and structure of heterostructures than that of one-step CVD method. Moreover with this method, the unique heterostructure with monolayer MoS₂ core wrapped by multilayer WS₂ are obtained, which is entirely different from the heterostructures synthesized by one-step CVD method. This approach may be extendable to the growth of various desirable heterojunctions or even superlattice consisting of other two-dimensional materials, which would provide an exciting platform for the next generation optoelectronic devices.

METHODS

Transfer the As-Grown Heterostructures onto the SiN TEM Grid. Transfer process is as follows: (1) a poly methyl methacrylate (PMMA) (3000 rpm for 1 min, 5%–9% wt, in anisole) was spin-coated; (2) the sample baked at 170 °C for 3–5 min; (3) the PMMA-capped sample then was put into the NaOH (2 M) solution at 100 °C for

1 h; (4) the floating film was dredged up with a clean glass substrate and transferred into DI water to remove the etchant ions; (5) the film was transferred onto a SiN TEM grid and dried on a hot plate (100 °C for 15 min); (6) the film was dipped into acetone to remove the PMMA layer and dried on a hot plate (50 °C for 10 min).

Device Fabrication. MoS₂–WS₂ p–n diodes device was fabricated by a fully dry photolithography-free process for the Au electrode preparation. The electrode was formed by tailoring a 100 nm thick Au film predeposited on another substrate. Subsequently, the electrode was tipped up by a micromanipulator, aligned to the heterostructure domain, and allocated under a 400× optical microscope.

Characterizations. Heterostructures were measured using commercially available Raman/PL spectrometer (Renishaw, Inc.) with 514 nm laser source. Raman and PL measurements were taken on a 1 μm² laser spot size with a power of 1 mW at room temperature. The KPFM and AFM images were taken with a Bruker Dimension Icon. SEM and TEM images were taken by LEO 1450VP and FEI TecnaiF20, respectively.

Conflict of Interest: The authors declare no competing financial interest.

Acknowledgment. The work is in part supported by Research Grants Council of Hong Kong, particularly, via Grant Nos. N_CUHK405/12, AoE/P-02/12, CUHK1/CRF/12G, CUHK142075E/15, and CUHK Group Research Scheme, as well as Innovation and Technology Commission ITS/096/14. J. B. Xu and W. G. Xie would like to thank the National Natural Science Foundation of China for the support, particularly, via Grant Nos. 61229401 and 11574119.

Supporting Information Available: The Supporting Information is available free of charge on the ACS Publications website at DOI: 10.1021/acsnano.5b03188.

Detailed parameters for the synthesis of monolayer MoS₂ nanosheets on SiO₂/Si substrate, a ring of protuberance interface between MoS₂ and WS₂ in MoS₂–WS₂ heterostructures (PDF)

REFERENCES AND NOTES

1. Han, G. H.; Rodriguez-Manzo, J. A.; Lee, C. W.; Kybert, N. J.; Lerner, M. B.; Qi, Z. J.; Dattoli, E. N.; Rappe, A. M.; Drndic, M.; Johnson, A. T. Continuous Growth of Hexagonal Graphene and Boron Nitride In-Plane Heterostructures by Atmospheric Pressure Chemical Vapor Deposition. *ACS Nano* **2013**, *7*, 10129–10138.
2. Mishchenko, A.; Tu, J. S.; Cao, Y.; Gorbachev, R. V.; Wallbank, J. R.; Greenaway, M. T.; Morozov, V. E.; Morozov, S. V.; Zhu, M. J.; Wong, S. L.; et al. Twist-Controlled Resonant Tunnelling in Graphene/Boron Nitride/Graphene Heterostructures. *Nat. Nanotechnol.* **2014**, *9*, 808–813.
3. Gao, T.; Song, X.; Du, H.; Nie, Y.; Chen, Y.; Ji, Q.; Sun, J.; Yang, Y.; Zhang, Y.; Liu, Z. Temperature-Triggered Chemical Switching Growth of In-Plane and Vertically Stacked Graphene-Boron Nitride Heterostructures. *Nat. Commun.* **2015**, *6*, 6835.
4. Ohno, Y.; Young, D. K.; Beschoten, B.; Matsukura, F.; Ohno, H.; Awschalom, D. D. Electrical Spin Injection in a Ferromagnetic Semiconductor Heterostructure. *Nature* **1999**, *402*, 790–792.
5. Faist, J.; Capasso, F.; Sivco, D. L.; Sirtori, C.; Hutchinson, A. L.; Cho, A. Y. Quantum Cascade Laser. *Science* **1994**, *264*, 553–556.
6. Wang, Q. H.; Kalantar-Zadeh, K.; Kis, A.; Coleman, J. N.; Strano, M. S. Electronics and Optoelectronics of Two-Dimensional Transition Metal Dichalcogenides. *Nat. Nanotechnol.* **2012**, *7*, 699–712.
7. Mak, K. F.; Lee, C.; Hone, J.; Shan, J.; Heinz, T. F. Atomically Thin MoS₂: A New Direct-Gap Semiconductor. *Phys. Rev. Lett.* **2010**, *105*, 136805.
8. Wang, H.; Yu, L.; Lee, Y. H.; Shi, Y.; Hsu, A.; Chin, M. L.; Li, L. J.; Dubey, M.; Kong, J.; Palacios, T. Integrated Circuits Based on Bilayer MoS(2) Transistors. *Nano Lett.* **2012**, *12*, 4674–4680.
9. Radisavljevic, B.; Radenovic, A.; Brivio, J.; Giacometti, V.; Kis, A. Single-Layer MoS₂ Transistors. *Nat. Nanotechnol.* **2011**, *6*, 147–150.
10. Liu, Z.; Ma, L.; Shi, G.; Zhou, W.; Gong, Y.; Lei, S.; Yang, X.; Zhang, J.; Yu, J.; Hackenberg, K. P.; et al. In-Plane Heterostructures of Graphene and Hexagonal Boron Nitride with Controlled Domain Sizes. *Nat. Nanotechnol.* **2013**, *8*, 119–124.
11. Zhang, X. Q.; Lin, C. H.; Tseng, Y. W.; Huang, K. H.; Lee, Y. H. Synthesis of Lateral Heterostructures of Semiconducting Atomic Layers. *Nano Lett.* **2015**, *15*, 410–415.
12. Gong, Y.; Lin, J.; Wang, X.; Shi, G.; Lei, S.; Lin, Z.; Zou, X.; Ye, G.; Vajtai, R.; Yakobson, B. I.; et al. Vertical and In-Plane Heterostructures from WS₂/MoS₂ Monolayers. *Nat. Mater.* **2014**, *13*, 1135–1142.
13. Huang, C.; Wu, S.; Sanchez, A. M.; Peters, J. J. P.; Beanland, R.; Ross, J. S.; Rivera, P.; Yao, W.; Cobden, D. H.; Xu, X. Lateral Heterojunctions within Monolayer MoSe₂–WSe₂ Semiconductors. *Nat. Mater.* **2014**, *13*, 1096–1101.
14. Duan, X.; Wang, C.; Shaw, J. C.; Cheng, R.; Chen, Y.; Li, H.; Wu, X.; Tang, Y.; Zhang, Q.; Pan, A.; et al. Lateral Epitaxial Growth of Two-Dimensional Layered Semiconductor Heterojunctions. *Nat. Nanotechnol.* **2014**, *9*, 1024–1030.
15. Liu, L.; Park, J.; Siegel, D. A.; McCarty, K. F.; Clark, K. W.; Deng, W.; Basile, L.; Idrobo, J. C.; Li, A. P.; Gu, G. Heteroepitaxial Growth of Two-Dimensional Hexagonal Boron Nitride Tempered by Graphene Edges. *Science* **2014**, *343*, 163–167.
16. Levendorf, M. P.; Kim, C. J.; Brown, L.; Huang, P. Y.; Havener, R. W.; Muller, D. A.; Park, J. Graphene and Boron Nitride Lateral Heterostructures for Atomically Thin Circuitry. *Nature* **2012**, *488*, 627–632.
17. Li, M. Y.; Shi, Y.; Cheng, C. C.; Lu, L. S.; Lin, Y. C.; Tang, H. L.; Tsai, M. L.; Chu, C. W.; Wei, K. H.; He, J. H.; et al. Epitaxial Growth of a Monolayer WSe₂–MoS₂ Lateral P–N Junction with an Atomically Sharp Interface. *Science* **2015**, *349*, 524–528.
18. Tripathy, P. K.; Chakraborty, S. P.; Sharma, I. G.; Bose, D. K. A Comparative Study on the Thermal Decomposition of Ammonium P-Tungstate in Batch and Fluidized-Bed Reactors. *Ind. Eng. Chem. Res.* **1997**, *36*, 3602–3606.
19. Lee, Y. H.; Zhang, X. Q.; Zhang, W.; Chang, M. T.; Lin, C. T.; Chang, K. D.; Yu, Y. C.; Wang, J. T.; Chang, C. S.; Li, L. J.; et al. Synthesis of Large-Area MoS₂ Atomic Layers with Chemical Vapor Deposition. *Adv. Mater.* **2012**, *24*, 2320–2325.
20. Li, H.; Zhang, Q.; Yap, C. C. R.; Tay, B. K.; Edwin, T. H. T.; Olivier, A.; Baillargeat, D. From Bulk to Monolayer MoS₂: Evolution of Raman Scattering. *Adv. Funct. Mater.* **2012**, *22*, 1385–1390.
21. Berkdemir, A.; Gutierrez, H. R.; Botello-Mendez, A. R.; Perea-Lopez, N.; Elias, A. L.; Chia, C. I.; Wang, B.; Crespi, V. H.; Lopez-Urias, F.; Charlier, J. C.; et al. Identification of Individual and Few Layers of WS₂ Using Raman Spectroscopy. *Sci. Rep.* **2013**, *3*, 1755.
22. Zhao, W.; Ghorannevis, Z.; Amara, K. K.; Pang, J. R.; Toh, M.; Zhang, X.; Kloc, C.; Tan, P. H.; Eda, G. Lattice Dynamics in Mono- and Few-Layer Sheets of WS₂ and WSe₂. *Nanoscale* **2013**, *5*, 9677–9683.
23. Gutierrez, H. R.; Perea-Lopez, N.; Elias, A. L.; Berkdemir, A.; Wang, B.; Lv, R.; Lopez-Urias, F.; Crespi, V. H.; Terrones, H.; Terrones, M. Extraordinary Room-Temperature Photoluminescence in Triangular WS₂ Monolayers. *Nano Lett.* **2013**, *13*, 3447–3454.
24. Iqbal, M. W.; Iqbal, M. Z.; Khan, M. F.; Shehzad, M. A.; Seo, Y.; Eom, J. Deep-Ultraviolet-Light-Driven Reversible Doping of WS₂ Field-Effect Transistors. *Nanoscale* **2015**, *7*, 747–757.
25. Ling, X.; Lee, Y. H.; Lin, Y.; Fang, W.; Yu, L.; Dresselhaus, M. S.; Kong, J. Role of the Seeding Promoter in MoS₂ Growth by Chemical Vapor Deposition. *Nano Lett.* **2014**, *14*, 464–472.
26. Rong, Y.; Fan, Y.; Leen Koh, A.; Robertson, A. W.; He, K.; Wang, S.; Tan, H.; Sinclair, R.; Warner, J. H. Controlling Sulphur Precursor Addition for Large Single Crystal Domains of WS₂. *Nanoscale* **2014**, *6*, 12096–12103.
27. Zhu, B.; Zeng, H.; Dai, J.; Gong, Z.; Cui, X. Anomalously Robust Valley Polarization and Valley Coherence in Bilayer WS₂. *Proc. Natl. Acad. Sci. U. S. A.* **2014**, *111*, 11606–11611.
28. Park, J.; Lee, W.; Choi, T.; Hwang, S. H.; Myoung, J. M.; Jung, J. H.; Kim, S. H.; Kim, H. Layer-Modulated Synthesis of Uniform Tungsten Disulfide Nanosheet Using Gas-Phase Precursors. *Nanoscale* **2015**, *7*, 1308–1313.

29. Hwang, W. S.; Remskar, M.; Yan, R. S.; Kose, T.; Park, J. K.; Cho, B. J.; Haensch, W.; Xing, H. L.; Seabaugh, A.; Jena, D. Comparative Study of Chemically Synthesized and Exfoliated Multilayer MoS₂ Field-Effect Transistors. *Appl. Phys. Lett.* **2013**, *102*, 102.
30. Sze, S. M.; Ng, K. K. *Physics of Semiconductor Devices*; John Wiley & Sons: Hoboken, NJ, 2007; pp 80–90.
31. Kang, J.; Sahin, H.; Peeters, F. M. Tuning Carrier Confinement in the MoS₂/WS₂ lateral Heterostructure. *J. Phys. Chem. C* **2015**, *119*, 9580–9586.
32. Wang, X. M.; Xu, J. B.; Xie, W. G.; Du, J. Quantitative Analysis of Graphene Doping by Organic Molecular Charge Transfer. *J. Phys. Chem. C* **2011**, *115*, 7596–7602.
33. Corovic, S.; Lackovic, I.; Sustaric, P.; Sustar, T.; Rodic, T.; Miklavcic, D. Modeling of Electric Field Distribution in Tissues During Electroporation. *Biomed. Eng. Online* **2013**, *12*, 16.
34. Ren, J.; McIsaac, K. A.; Patel, R. V.; Peters, T. M. A Potential Field Model Using Generalized Sigmoid Functions. *IEEE Trans. Syst. Man Cybern. B Cybern.* **2007**, *37*, 477–484.
35. Cudazzo, P.; Tokatly, I. V.; Rubio, A. Dielectric Screening in Two-Dimensional Insulators: Implications for Excitonic and Impurity States in Graphane. *Phys. Rev. B: Condens. Matter Mater. Phys.* **2011**, *84*, 085406.
36. Lin, Y.; Ling, X.; Yu, L.; Huang, S.; Hsu, A. L.; Lee, Y. H.; Kong, J.; Dresselhaus, M. S.; Palacios, T. Dielectric Screening of Excitons and Trions in Single-Layer MoS₂. *Nano Lett.* **2014**, *14*, 5569–5576.
37. Kumar, A.; Ahluwalia, P. K. Tunable Dielectric Response of Transition Metals Dichalcogenides M_xS₂ (M = Mo, W; X = S, Se, Te): Effect of Quantum Confinement. *Phys. B* **2012**, *407*, 4627–4634.
38. Berkelbach, T. C.; Hybertsen, M. S.; Reichman, D. R. Theory of Neutral and Charged Excitons in Monolayer Transition Metal Dichalcogenides. *Phys. Rev. B: Condens. Matter Mater. Phys.* **2013**, *88*, 045318.
39. Lee, Y. H.; Yu, L.; Wang, H.; Fang, W.; Ling, X.; Shi, Y.; Lin, C. T.; Huang, J. K.; Chang, M. T.; Chang, C. S.; et al. Synthesis and Transfer of Single-Layer Transition Metal Disulfides on Diverse Surfaces. *Nano Lett.* **2013**, *13*, 1852–1857.